

# Transonic Wing Optimization by Variable-resolution Modeling and Space Mapping

Eirikur Jonsson, Leifur Leifsson and Slawomir Koziel

*Engineering Optimization & Modeling Center, School of Science and Engineering, Reykjavik University, Reykjavik, Iceland*

**Keywords:** Transonic Wing Design, CFD, Surrogate-based Optimization, Variable-resolution Modeling, Space Mapping.

**Abstract:** This paper presents an efficient aerodynamic design optimization methodology for wings in transonic flow. The approach replaces the computationally expensive high-fidelity CFD model in an iterative optimization process with a corrected polynomial approximation model constructed by a cheap low-fidelity CFD model. The output space mapping technique is used to correct the approximation model to yield an accurate predictor of the high-fidelity one. Both CFD models employ the RANS equations with the Spalart-Allmaras turbulence model, but the low-fidelity one uses a coarse mesh resolution and relaxed convergence criteria. Our method is applied to a constrained lift maximization of a rectangular wing at transonic conditions with 3 design variables. The optimized designs are obtained by using 50 low-fidelity CFD model evaluations to set up the approximation model and 7 to 8 high-fidelity model evaluations, equivalent to around 10 high-fidelity CFD model evaluations.

## 1 INTRODUCTION

The wing is the most important component of an aircraft, significantly affecting its overall performance. As the wing provides lift, it is at the same time the main source of drag, responsible for about 2/3 of the total drag of the aircraft (Raymer, 2006). Reducing this wing drag by a better design, and, hence, minimizing cost, is often the primary objective of modern aircraft design.

Nowadays, aerodynamic design using high-fidelity computational fluid dynamic (CFD) models is ubiquitous and plays an important role in aircraft development. Traditional design optimization techniques, such as gradient-based or population-based ones, involve a large number of simulations. Consequently, direct aerodynamic optimization with high-fidelity CFD models using traditional optimization techniques is impractical, even when using cheap adjoint sensitivities.

One of the overall objectives of surrogate-based optimization (SBO) (Queipo et al., 2005; Forrester and Keane, 2009) is to reduce the number of evaluations of expensive simulations, thereby making the design process more efficient. This is achieved by an iterative correction-prediction process where a surrogate model (a computationally cheap representation of the high-fidelity one) is constructed and subsequent

exploited to obtain approximate location of the high-fidelity model optimal design. The surrogate model can be constructed by approximating sampled high-fidelity model data using, e.g., polynomial approximation (Queipo et al., 2005), radial basis functions (Forrester and Keane, 2009; Wild et al., 2008), kriging (Koziel et al., 2011; Simpson et al., 2001; Journel and Huijbregts, 1978; O'Hagan and Kingman, 1978), neural networks (Haikin, 1998; Minsky and Papert, 1969), or support vector regression (Smola and Schölkopf, 2004) (response surface approximation surrogates) or by correcting/enhancing a physics-based low-fidelity model (physical surrogates) (Søndergaard, 2003).

Approximation surrogates usually require a significant number of high-fidelity model evaluations to ensure decent accuracy. Furthermore, the number of samples typically grows exponentially with the number of design variables. On the other hand, approximation surrogates can be a basis of efficient global optimization techniques (Forrester and Keane, 2009). Various techniques of updating the training data set (so-called infill criteria (Forrester and Keane, 2009)) have been developed that aim at obtaining global modeling accuracy, locating globally optimal design, or the trade-offs between the two, particularly in the context of kriging interpolation (Forrester and Keane, 2009).

Physics-based surrogate models are not as versatile as approximation ones because they rely on an underlying low-fidelity model (a simplified description of the system under consideration), typically problem specific. The physics-based models can be obtained by a number of ways, such as by neglecting certain second-order effects, using simplified equations, or, which is probably the most versatile approach, by exploiting the same CFD solver as used to evaluate the high-fidelity model but with coarser mesh and/or relaxed convergence criteria (so called variable-resolution modeling) (Leifsson and Koziel, 2011b). The physics-based surrogate models contain knowledge about the system of interest. Due to this, a limited amount of high-fidelity model data is necessary to ensure a required accuracy of the surrogate. For the same reason, these physics-based models have good generalization capabilities.

There have been proposed several SBO algorithms using physics-based surrogates in the literature, including the approximation and model management optimization (AMMO) (Alexandrov and Lewis, 2001), space mapping (SM) (Bandler et al., 2004; Koziel et al., 2008), manifold mapping (MM) (Echeverria and Hemker, 2005), and, more recently, the shape-preserving response prediction (SPRP) (Leifsson and Koziel, 2011a). All of these methods differ in a specific way of how the low-fidelity model is used to construct the surrogate. Space mapping is probably the most popular approach of this kind. It was originally developed for simulation-driven design in microwave engineering (Bandler et al., 2004) however, it is currently becoming more and more popular in other areas of engineering and science (cf. Refs. (Bandler et al., 2004; Koziel et al., 2008), and references therein). Despite its potential, space mapping has not become popular in aerodynamic shape optimization. The only work reported so far is by Robinson et al. (Robinson et al., 2006), where the so-called corrected SM was applied, among other methods, to airfoil design, however no significant design speed up has been reported.

In this paper, we develop a space mapping algorithm for the aerodynamic design optimization of wings in transonic flow. In particular, we extend our recently developed algorithm for airfoils in two-dimensional transonic flow (Koziel and Leifsson, 2012) which employed variable-resolution models and output space mapping (Bandler et al., 2004; Koziel et al., 2008). The algorithm proposed in this work handles three-dimensional flow past wings. The complicated fluid flow analysis includes a certain level of numerical noise. To overcome associated problems, we have replaced the direct use of low-

fidelity models by approximation models. We demonstrate the effectiveness of the algorithm by a couple of numerical examples involving constrained lift maximization.

## 2 CFD MODELING

In this section, we present the CFD model. In particular, the governing equations, geometry and grid generation are presented. We, furthermore, present the results of a grid convergence study and model validation.

### 2.1 Governing Equations

Commercial transport aircraft operate in the transonic flow regime where the flow is compressible. We assume that the fluid is air modelled by the ideal gas law and the Sutherland law for dynamic viscosity  $\mu$ . The flow is assumed to be steady, viscous, and without body forces, mass-diffusion, chemical reactions or external heat addition. We solve the RANS equations with the one equation Spalart-Allmaras turbulence model (Tannehill et al., 1997).

### 2.2 Wing Geometry

In this work, we consider a simple constant chord wing. The wing is constructed by two NACA four digit airfoils (Abbott and Von Doenhoff, 1959), one at the root and the other at the tip as shown in Fig. 1. Three parameters define each airfoil section, namely the maximum ordinate of the mean camberline as a fraction of chord ( $m$ ), the chordwise position of the maximum ordinate ( $p$ ), and the thickness-to-chord ratio ( $t/c$ ) (see Abbott and von Doenhoff (Abbott and Von Doenhoff, 1959) for details). The reason for choosing these particular airfoils and the wing geometry is to limit the number of design variables in our initial study.

### 2.3 Computational Grid

The farfield is configured in a box topology where the wing root airfoil is placed in the center of the symmetry plane with its leading edge placed at the origin  $(x,y,z) = (0,0,0)$ . The farfield extends 100 chord lengths,  $100c$ , in all directions from the wing, upstream, above, below and aft of the wing where the maximum element size in the flow domain is 11 chord lengths or  $11c$ . The computational domain is shown in Fig. 2.

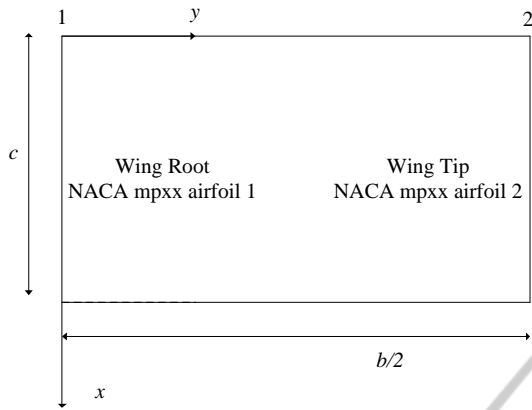


Figure 1: A planform view of a constant chord wing used in this work. The rectangular wing is constructed by two NACA airfoils, shown at spanstations 1, the wing root, and 2, the wing tip. Each airfoil has its own set of design parameters. The wing semispan is  $b/2$ .

An unstructured tri/tetra shell grid is created on all surfaces. The shell grid from the wing is then extruded into the volume where the volume is flooded with tri/tetra elements. The grid is made dense close to the wing where it then gradually grows in size as moving away from the wing surfaces. To capture the viscous boundary layer an inflation layer or a prism layer is created on the wing surfaces as well. In the stream-wise direction, the number of elements on the wing is set to 100 on both upper and lower surface. The bi-geometric bunching law with a growth ratio of 1.2 is employed in the stream-wise direction over the wing to obtain a more dense element distribution at the leading edge and the trailing edge. This is done in order to capture the high pressure gradient at the leading edge and the separation at the trailing edge. The minimum element size of the wing in the stream-wise direction is set to  $0.1\%c$ , and it is located at the leading and trailing edge. In the span-wise direction elements are distributed uniformly and number of elements set to 100 over the semi-span. A prism layer is used to capture the viscous boundary layer. This layer consists of a number of structured elements that grow in size normal to the wing surface into the domain volume. The inflation layer has a initial height of  $5 \times 10^{-6}c$  where it is grown 20 layers into the volume using a exponential growth law with ratio of 1.2. The initial layer height is chosen so that  $y^+ < 1$  at all nodes on the wing. The resulting grid is shown in Fig. 3.

### 2.4 Flow Solver

The numerical fluid flow simulations are performed using the computer code ANSYS FLUENT (ANSYS,

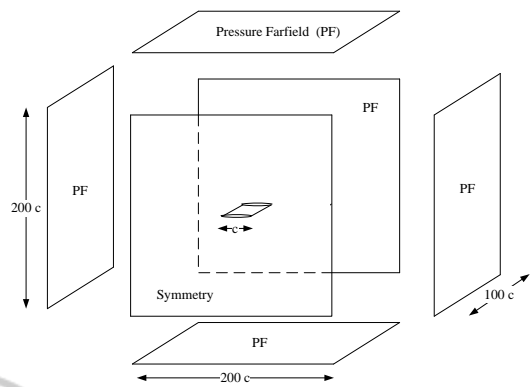


Figure 2: A sketch of the computational domain. All boundaries are set as pressure-farfield (PF), a side from the wing surface, which is a wall type. Symmetry is applied through the wing center. The wing chord length is denoted by  $c$ .

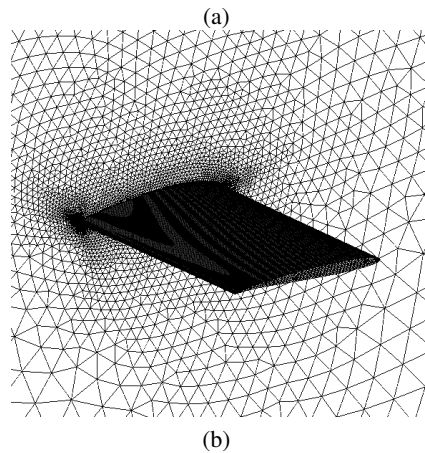
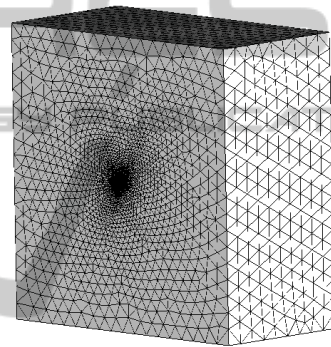


Figure 3: A view of of the computational grid, (a) the farfield grid, and (b) a close-up of the wing shell grid.

2010). The implicit density-based solver is applied using the Roe-FDS flux type. The spatial discretization schemes are set to second order for all variables, and the gradient information is found using the Green-Gauss node based method. The residuals, which are the sum of the  $L^2$  norm of all governing

equations in each cell, are monitored and checked for convergence. The convergence criterion for the high-fidelity model is such that a solution is considered to be converged if the residuals have dropped by six orders of magnitude, or the total number of iterations has reached 1000. Also, the lift and drag coefficients are monitored for convergence.

To reflect the compressible nature of this problem, two types of boundaries are used. The pressure-farfield is applied to the boundary on all surfaces, except where the wing penetrates the symmetry boundary. The boundary types is shown in Fig. 2.

Air is the working fluid at compressible transonic conditions. The free-stream Reynolds number is  $Re_{\infty,S} = 11.72 \times 10^6$ , where  $S$  is the reference area, which in this case is planform area. The Mach number is set to  $M_{\infty} = 0.8395$  and the angle of attack is set to  $\alpha = 0^\circ$ . We assume that the flow is calm at its boundaries and turbulent viscosity ratio set to  $\mu_t/\mu_{\infty} = 1$ . Furthermore, the boundary pressure and temperature is set to  $p_{\infty} = 80507.2 Pa$  and  $T_{\infty} = 255.6 K$ .

## 2.5 Grid Convergence

A grid convergence study is conducted using the ONERA M6 wing (NASA, 2008). The flow past the ONERA M6 wing is simulated at various grid resolutions at  $Re_{\infty,c_{mac}} = 11.72 \times 10^6$ ,  $M_{\infty} = 0.8395$  and angle of attack  $\alpha = 3.06^\circ$ , where  $c_{mac}$  is the mean aerodynamic chord length. The flow conditions are selected to match experimental flow conditions of an ONERA M6 wing experiment 2308 conducted by Schmitt, V. and F. Charpin (Schmitt and Charpin, 1979), see Section 2.6.

The grid convergence study shown in Fig. 4(a) revealed that 1,576,413 cells are needed for convergence in lift. The drag, however, can still be improved as evident from Fig. 4(a), where convergence has not been reached due to limitations in the computational resources. We proceed, however, with this grid as the high-fidelity model grid. The overall simulation time needed for one high-fidelity CFD simulation was around 223 minutes, as shown in Fig. 4(b), executed on four Intel-i7-2600 processors in parallel. This execution time is based on 1000 solver iterations, where the solver terminated due to the maximum number of iterations limit.

## 2.6 Model Validation

The ONERA M6 wing is a commonly used CFD validation case for external flows because of its simple geometry combined with complexities of transonic flow, i.e., local supersonic flow, shocks, and turbu-

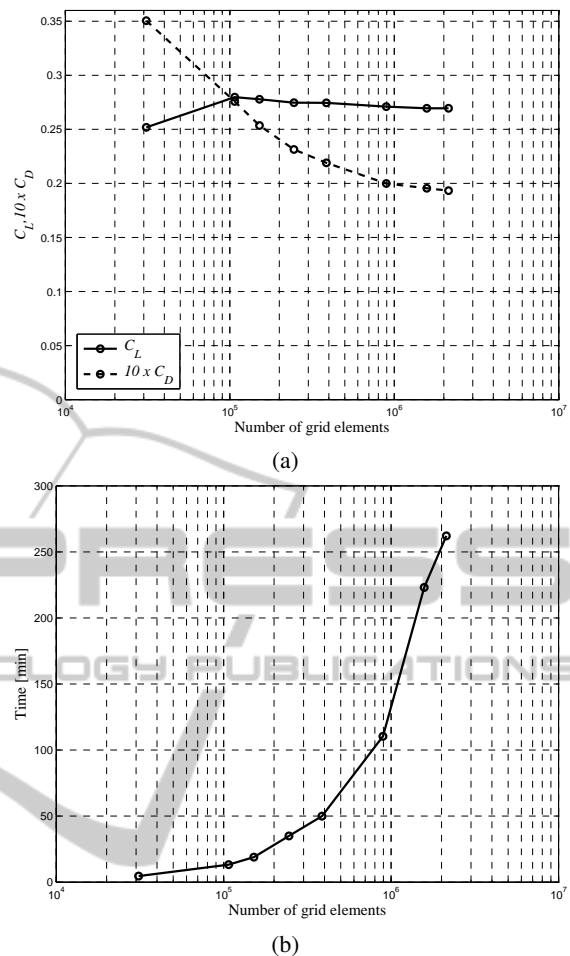


Figure 4: Grid convergence study using the ONERA M6 wing at  $Re_{\infty,c_{mac}} = 11.72 \times 10^6$ ,  $M_{\infty} = 0.8395$  and angle of attack  $\alpha = 3.06^\circ$ . (a) Lift ( $C_L$ ) and drag ( $C_D$ ) coefficients versus the number of grid elements, and (b) simulation time versus the number of grid elements.

lent boundary layers with separation. We consider the ONERA M6 wing as a validation case for the high-fidelity CFD model. The ONERA M6 wing is a swept, semi-span wing with no twist and then symmetrical ONERA D airfoil section (Schmitt and Charpin, 1979). The numerical coordinates of the airfoil section at the  $y/(b/2) = 0$  are obtained from NASA (NASA, 2008). The coordinates indicate that there is a finite thickness to the trailing edge. In this work, we use a zero trailing edge thickness. The airfoil coordinates are linearly scaled near the trailing edge so that the trailing edge thickness is zero. We use experimental data from a ONERA M6 wing wind tunnel experiment 2308 conducted by Schmitt, V. and F. Charpin (Schmitt and Charpin, 1979). The solver is configured to match the experimental flow conditions which are  $Re_{\infty,c_{mac}} = 11.72 \times 10^6$ ,  $M_{\infty} = 0.8395$ , angle of attack  $\alpha = 3.06^\circ$ , pressure  $p_{\infty} = 80507.2 Pa$  and

temperature  $T_\infty = 255.6K$ .

The available experimental data obtained by Schmitt and Charpin, consists of pressure distributions ( $C_p$ ) at seven cross-sections along the span, namely,  $y/(b/2) = 0.2, 0.44, 0.65, 0.8, 0.9, 0.95, 0.99$ . The CFD simulation results are shown for  $y/(b/2) = 0.2, 0.65, 0.95$ , in Fig. 5. Inspecting the results, we see that the correlation between the CFD simulation and experimental data is excellent.

### 3 OPTIMIZATION WITH SPACE MAPPING

In this paper, the wing design is carried out in a computationally efficient manner by exploiting the space mapping (SM) methodology (Bandler et al., 2004). Space mapping replaces the direct optimization of an expensive (high-fidelity or fine) airfoil model  $f$  obtained through high-fidelity CFD simulation, by an iterative updating and re-optimization of a cheaper surrogate model  $s$ . The key component of SM is the physics-based low-fidelity (or coarse) model  $c$  that embeds certain knowledge about the system under consideration and allows us to construct a reliable surrogate using a limited amount of high-fidelity model data. Here, the low-fidelity model is evaluated using the same CFD solver as the high-fidelity one, so that both models share the same knowledge of the wing performance.

#### 3.1 Optimization Problem

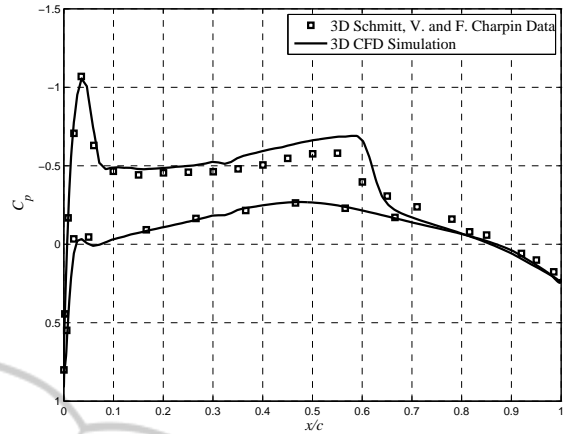
The simulation-driven design can be generally formulated as a nonlinear minimization problem

$$\mathbf{x}^* = \arg \min_{\mathbf{x}} H(f(\mathbf{x})), \quad (1)$$

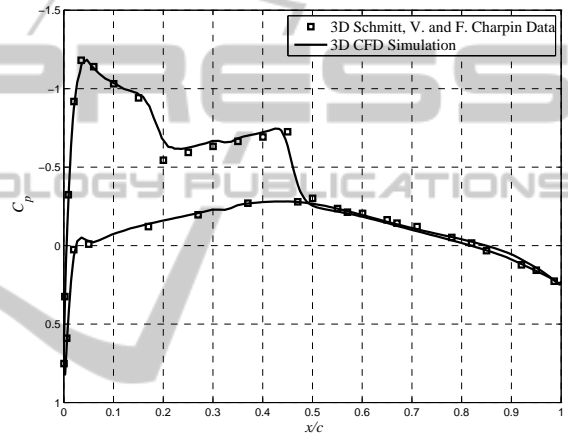
where  $\mathbf{x}$  is a vector of design parameters,  $f$  the high-fidelity model to be minimized at  $\mathbf{x}$  and  $H$  is the objective function.  $\mathbf{x}^*$  is the optimum design vector. The high-fidelity model will represent aerodynamic forces, lift and drag coefficient, as well as other scalar responses such as cross-sectional area  $A$  of the wing at interesting location. Area response can be of a vector form  $\mathbf{A}$  if one requires multiple area cross-sectional constraints at various locations on the wing, e.g., the wing root and the wing tip. The response will have to form

$$f(\mathbf{x}) = [C_{L,f}(\mathbf{x}), C_{D,f}(\mathbf{x}), A_f(\mathbf{x})]^T, \quad (2)$$

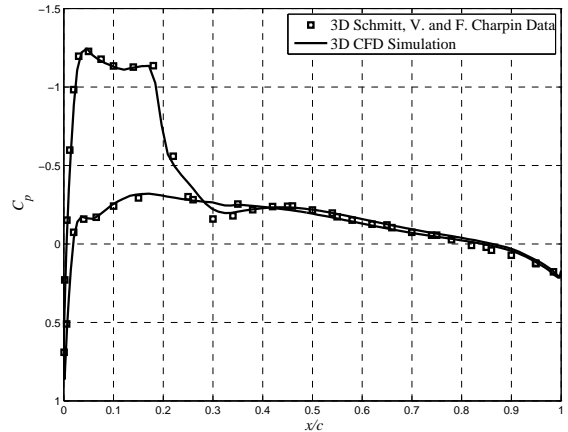
where  $C_{L,f}$  and  $C_{D,f}$  are the lift and drag coefficient for a three-dimensional wing, respectively, generated by the high-fidelity model. We are interested in the



(a)  $y/(b/2) = 0.2$ .



(b)  $y/(b/2) = 0.65$ .



(c)  $y/(b/2) = 0.95$ .

Figure 5: Pressure distributions ( $C_p$ ) at  $y/(b/2) =$  (a) 0.2; (b) 0.65 (c) 0.95 of the ONERA M6 wing at  $M_\infty = 0.8395$  and angle of attack  $\alpha = 3.06^\circ$ . The CFD simulation results are shown with a solid line (-). The wind tunnel experimental data (from Schmitt, V. and F. Charpin (Schmitt and Charpin, 1979)) is shown with square markers.

maximizing lift case, so the objective function will take the form of

$$H(f(\mathbf{x})) = -C_L, \quad (3)$$

the design constraints denoted as

$$C(f(\mathbf{x})) = [c_1(f(\mathbf{x})), \dots, c_k(f(\mathbf{x}))]^T. \quad (4)$$

Maximizing lift will yield two nonlinear design constraints for drag and area,

$$c_1(f(\mathbf{x})) = C_{D,f}(\mathbf{x}) - C_{D,\max} \leq 0, \quad (5)$$

$$c_2(f(\mathbf{x})) = -A_f(\mathbf{x}) + A_{\min} \leq 0. \quad (6)$$

where  $C_{D,\max}$  and  $A_{\min}$  are the maximum allowable drag and minimum allowable cross-sectional area, respectively.

### 3.2 Space Mapping Basics

Starting from an initial design  $\mathbf{x}^{(0)}$ , the generic space mapping algorithm produces a sequence  $\mathbf{x}^{(i)}, i = 0, 1 \dots$  of approximate solutions to Eq. (1) as

$$\mathbf{x}^{(i+1)} = \arg \min_{\mathbf{x}} H(s^{(i)}(\mathbf{x})), \quad (7)$$

where

$$s^{(i)}(\mathbf{x}) = [C_{L,s}^{(i)}(\mathbf{x}), C_{D,s}^{(i)}(\mathbf{x}), A_s(\mathbf{x})^{(i)}]^T, \quad (8)$$

is the surrogate model at iteration  $i$ . As previously described, the accurate high-fidelity CFD model  $f$  is accurate but computationally expensive. Using space mapping, the surrogate  $s$  is a composition of the low-fidelity CFD model  $c$  and a simple linear transformation to correct the low-fidelity model response (Bandler et al., 2004). The corrected response is denoted as  $s(\mathbf{x}, \mathbf{p})$ , where  $\mathbf{p}$  represents a set of model parameters and at iteration  $i$  the surrogate is

$$s^{(i)}(\mathbf{x}) = s(\mathbf{x}, \mathbf{p}). \quad (9)$$

The SM parameters  $\mathbf{p}$  are determined through a parameter extraction (PE) process. In general, this process is a nonlinear optimization problem where the objective is to minimize the misalignment of surrogate response at some or all previous iteration high-fidelity model data points (Bandler et al., 2004). The PE optimization problem can be defined as

$$\mathbf{p}^{(i)} = \arg \min_{\mathbf{p}} \sum_{k=0}^i w_{i,k} \|f(\mathbf{x}^{(k)}) - s(\mathbf{x}^{(k)}, \mathbf{p})\|^2, \quad (10)$$

where  $w_{i,k}$  are weight factors that control how much impact previous iterations affect the SM parameters. Popular choices are

$$w_{i,k} = 1 \quad \forall i, k, \quad (11)$$

and

$$w_{i,k} = \begin{cases} 1 & k = i \\ 0 & \text{otherwise} \end{cases}. \quad (12)$$

In the first case, all previous SM iterations influence the parameters; in the second case, the parameters depend only on the most recent SM iteration.

### 3.3 Low-fidelity CFD Model

The low-fidelity model  $c$  is constructed in the same way as the high-fidelity model  $f$ , but with a coarser grid discretization and with a relaxed convergence criteria - the so called variable-resolution modeling. Referring back to the grid study made in Section 2.5 and inspecting Fig. 4(a), we make our selection for the coarse low-fidelity model. Based on time and accuracy with respect of lift and drag, we select the grid parameters that represent the second point from left, giving a 107,054 elements. The time taken to evaluate the low-fidelity model is 13.2 minutes on four Intel-i7-2600 processors in parallel. Inspecting further the lift and drag convergence plot for the low-fidelity model in Fig. 6, we note that the solution has converged after 400-500 iterations. The maximum number of iterations for the low-fidelity model is therefore set to 500 iterations. This reduces the overall simulation time to 6.6 minutes. The ratio of simulation times of the high- and low- fidelity model in this case is high/low = 223/6.6  $\approx$  34. This is based on the solver uses all 500 iterations in the low-fidelity model to obtain a solution.

The low-fidelity CFD model  $c$  turns out to be very noisy. In order to alleviate the problem, a second order polynomial approximation model is constructed (Koziel et al., 2011) using  $N_c = 50$  training points sampled using latin hypercube sampling (LHS) (Forrester and Keane, 2009) using the low-fidelity CFD model. The polynomial approximation model is defined as

$$\bar{c}(\mathbf{x}) = c_0 + \mathbf{c}_1^T \mathbf{x} + \mathbf{x}^T \mathbf{c}_2 \mathbf{x}, \quad (13)$$

where  $\mathbf{c}_1 = [c_{1.1} \quad c_{1.2} \quad c_{1.3}]^T$  and  $\mathbf{c}_2 = [c_{2.ij}]_{i,j=1,2,3}$ . The coefficients  $c_0, \mathbf{c}_1, \mathbf{c}_2$  are found by solving a linear regression problem

$$\bar{c}(\mathbf{x}^k) = c(\mathbf{x}^k), \quad (14)$$

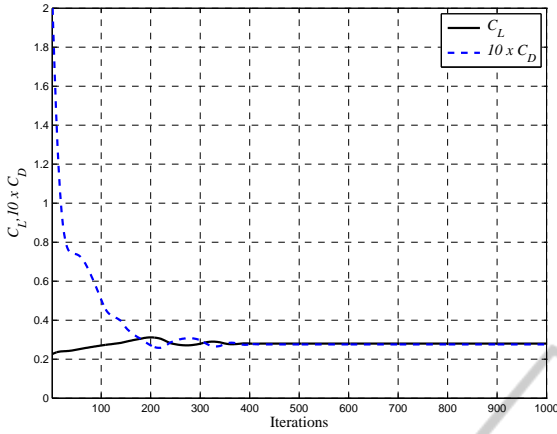


Figure 6: Lift and drag coefficient convergence plot for the low-fidelity model obtained in the grid convergence study using the ONERA M6 wing at Mach number  $M_\infty = 0.8395$  and angle of attack  $\alpha = 3.06^\circ$ .

where  $k = 1, \dots, N_c$ . The resulting second order polynomial model  $\bar{c}$  has nice analytical properties, such as smoothness and convexity.

### 3.4 Surrogate Model Construction

As mentioned above, the SM surrogate model  $s$  is a composition of the low-fidelity CFD model  $c$  and corrections or linear transformations where the model parameters  $\mathbf{p}$  are extracted using one of the PE processes described above. The parameter extraction and the surrogate optimization create a certain overhead on the whole process and this overhead can be up to 80-90 % of the computational cost. This is due to the fact that the physics-based low-fidelity models are in general relatively expensive to evaluate compared to the functional-based ones. Despite this, SM may be beneficial (Zhu et al., 2007).

To alleviate this problem, the output SM with both multiplicative and additive response correction is exploited here with the surrogate model parameters extracted analytically. We use the following formulation

$$s^{(i)}(\mathbf{x}) = \mathbf{A}^{(i)} \circ \bar{c}(\mathbf{x}) + \mathbf{D}^{(i)} + \mathbf{q}^{(i)} \quad (15)$$

or

$$s^{(i)}(\mathbf{x}) = \begin{bmatrix} a_L^{(i)} C_{L,c}(\mathbf{x}) + d_L^{(i)} + q_L^{(i)}, \\ a_D^{(i)} C_{D,c}(\mathbf{x}) + d_D^{(i)} + q_D^{(i)}, \quad A_c(\mathbf{x}) \end{bmatrix}^T, \quad (16)$$

where  $\circ$  is a component-wise multiplication. No mapping is needed for the area  $A_c(\mathbf{x})$  where,  $A_c(\mathbf{x}) = A_f(\mathbf{x}) \quad \forall \mathbf{x}$  since low- and high-fidelity model represent the same geometry. Parameters  $\mathbf{A}^{(i)}$  and  $\mathbf{D}^{(i)}$  are obtained using

$$[\mathbf{A}^{(i)}, \mathbf{D}^{(i)}] = \arg \min_{\mathbf{A}, \mathbf{D}} \sum_{k=0}^i \|f(\mathbf{x}^{(k)}) - \mathbf{A} \circ \bar{c}(\mathbf{x}^{(k)}) + \mathbf{D}\|^2, \quad (17)$$

where  $w_{i,k} = 1$ , i.e., all the previous iteration points are used to improve globally the response of the low-fidelity model. The additive term  $q^{(i)}$  is defined such that it ensures a perfect match between the surrogate and the high-fidelity model at design  $\mathbf{x}^{(i)}$ , namely  $f(\mathbf{x}^{(i)}) = s(\mathbf{x}^{(i)})$  or a zero-order consistency (Alexandrov and Lewis, 2001). We can write the additive term as

$$q^{(i)} = f(\mathbf{x}^{(i)}) - [\mathbf{A}^{(i)} \circ \bar{c}(\mathbf{x}^{(i)}) + \mathbf{D}^{(i)}]. \quad (18)$$

Since analytical solution exists for  $\mathbf{A}^{(i)}, \mathbf{D}^{(i)}$  and  $q^{(i)}$  there is no need for non-linear optimization for solving Eq. (10) to obtain the parameters. We can obtain  $\mathbf{A}^{(i)}$  and  $\mathbf{D}^{(i)}$  by solving

$$\begin{bmatrix} a_L^{(i)} \\ d_L^{(i)} \end{bmatrix} = (\mathbf{C}_L^T \mathbf{C}_L)^{-1} \mathbf{C}_L^T \mathbf{F}_L, \quad (19)$$

$$\begin{bmatrix} a_D^{(i)} \\ d_D^{(i)} \end{bmatrix} = (\mathbf{C}_D^T \mathbf{C}_D)^{-1} \mathbf{C}_D^T \mathbf{F}_D, \quad (20)$$

where

$$\mathbf{C}_L = \begin{bmatrix} C_{L,c}(\mathbf{x}^{(0)}) & C_{L,c}(\mathbf{x}^{(1)}) & \dots & C_{L,c}(\mathbf{x}^{(i)}) \\ 1 & 1 & \dots & 1 \end{bmatrix}^T, \quad (21)$$

$$\mathbf{F}_L = \begin{bmatrix} C_{L,f}(\mathbf{x}^{(0)}) & C_{L,f}(\mathbf{x}^{(1)}) & \dots & C_{L,f}(\mathbf{x}^{(i)}) \\ 1 & 1 & \dots & 1 \end{bmatrix}^T, \quad (22)$$

$$\mathbf{C}_D = \begin{bmatrix} C_{D,c}(\mathbf{x}^{(0)}) & C_{D,c}(\mathbf{x}^{(1)}) & \dots & C_{D,c}(\mathbf{x}^{(i)}) \\ 1 & 1 & \dots & 1 \end{bmatrix}^T, \quad (23)$$

$$\mathbf{F}_D = \begin{bmatrix} C_{D,f}(\mathbf{x}^{(0)}) & C_{D,f}(\mathbf{x}^{(1)}) & \dots & C_{D,f}(\mathbf{x}^{(i)}) \\ 1 & 1 & \dots & 1 \end{bmatrix}^T, \quad (24)$$

which are the least-square optimal solutions to the linear regression problems

$$\mathbf{C}_L a_L^{(i)} + d_L^{(i)} = \mathbf{F}_L, \quad (25)$$

$$\mathbf{C}_D a_D^{(i)} + d_D^{(i)} = \mathbf{F}_D. \quad (26)$$

Note that  $\mathbf{C}_L^T \mathbf{C}_L$  and  $\mathbf{C}_D^T \mathbf{C}_D$  are non-singular for  $i > 1$  and assuming that  $\mathbf{x}^{(k)} \neq \mathbf{x}^{(i)}$  for  $k \neq i$ . For  $i = 1$  only the multiplicative SM correction with  $\mathbf{A}^{(i)}$  is used.

### 3.5 Optimization Algorithm

Here, we formulate the optimization algorithm exploiting the SM based surrogate and a trust-region convergence safeguard (Forrester and Keane, 2009). The trust-region parameter  $\lambda$  is updated after each iteration. This algorithm will be used in applications presented in this thesis. The optimization algorithm is as follows:

1. Set  $i = 0$ ; Select  $\lambda$ , the trust region radius; Evaluate the high-fidelity model at the initial solution,  $f(\mathbf{x}^{(0)})$ ;
2. Using data from the low-fidelity model  $\bar{c}$ , and  $f$  at  $\mathbf{x}^{(k)}, k = 0, 1, \dots, i$ , setup the SM surrogate  $s^{(i)}$ ; Perform PE;
3. Optimize  $s^{(i)}$  to obtain  $\mathbf{x}^{(i+1)}$ ;
4. Evaluate  $f(\mathbf{x}^{(i+1)})$ ;
5. If  $H(f(\mathbf{x}^{(i+1)})) < H(f(\mathbf{x}^{(i)}))$ , accept  $\mathbf{x}^{(i+1)}$ ; Otherwise set  $\mathbf{x}^{(i+1)} = \mathbf{x}^{(i)}$ ;
6. Update  $\lambda$ ;
7. Set  $i = i + 1$ ;
8. If the termination condition is not satisfied, go to 2, else proceed;
9. End; Return  $\mathbf{x}^{(i)}$  as the optimum solution.

The termination condition is set to  $\|\mathbf{x}^{(i)} - \mathbf{x}^{(i-1)}\| < 10^{-3}$ .

## 4 NUMERICAL EXAMPLES

In this section, we apply the proposed optimization algorithm to the lift maximization of a rectangular wing at transonic conditions. The direct solution of the original problem in Eq. (1) has not been attempted due to the heavy computational cost of the high-fidelity model. We formulate the problem and describe the setup. Then, we present the results of numerical optimization.

### 4.1 Setup

The wing is unswept and untwisted and is constructed by two NACA 4 digit airfoils, located at the root and tip, as described in Fig. 1. The root airfoil is fixed to be NACA 2412. The tip airfoil is to be designed. The initial design  $\mathbf{x}^{(0)}$  for the wing tip is chosen at random at the start of each optimization run. The normalized semi-wingspan is set as twice the wing chord length  $c$  as  $(b/2) = 2c$ . All other wing parameters are kept fixed. The design vector can be written

as  $\mathbf{x} = [m, p, t/c]^T$ , where the variables represent the wing tip NACA 4 digit airfoil parameters.

The objective is to maximize the lift coefficient  $C_{L,f}$  subject to constraints on the drag coefficient  $C_{D,f} \leq C_{D,\max} = 0.03$  and the wing tip normalized cross-sectional area  $A \geq A_{\min} = 0.01$ . The side constraints on the design variables are  $0.02 \leq m \leq 0.03$ ,  $0.7 \leq p \leq 0.9$  and  $0.06 \leq t/c \leq 0.08$ .

### 4.2 Results

Two optimization runs were performed, denoted as Run 1 and Run 2. The numerical results are given in Table 1, and the initial and optimized airfoil cross-sections are shown in Fig. 7(a) and Fig. 7(b), respectively.

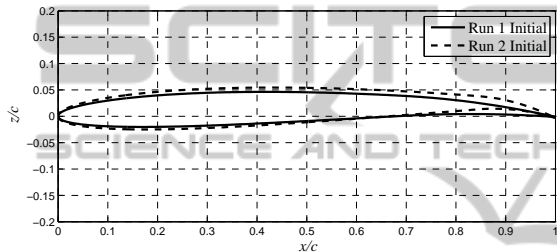
In Run 1, the lift is increased by +10% and the drag is pushed above its constraint at  $C_{D,\max} = 0.03$ , where the optimized drag coefficient is  $C_D = 0.0311$ . The drag constraint is violated slightly, or by +4%, which is within the 5% constraint tolerance band. The lift-to-drag ratio is decreased by -14%. The proposed method requires less than 10 high-fidelity model evaluations, where 50 low-fidelity model evaluations are used to create the approximation model and 8 high-fidelity model evaluations for each design iteration. It is evident that the optimized wing tip airfoil is thicker as the normalized cross-sectional area is increased by +26%, and the increased drag can be related to the increment in area. No change is in the camber  $m$ , but the location of the maximum camber  $p$  has moved slightly aft.

The initial design for Run 2 violates the drag constraint. The proposed method is, however, able to push the drag to its constraint limit where the optimized drag coefficient is slightly violated, by +2%. While the drag is decreased by -11%, the lift is maintained and only drops by -1%. As a result, the lift-to-drag ratio is increased by +11%. The proposed method requires less than 9 high-fidelity model evaluations (50 low-fidelity model evaluations used to create the approximation model and 7 high-fidelity model evaluations). The optimized wing tip airfoil is thinner than the initial design (the normalized cross-sectional area is reduced by -20%). Little changes are made to the camber  $m$  and the maximum camber location  $p$ .

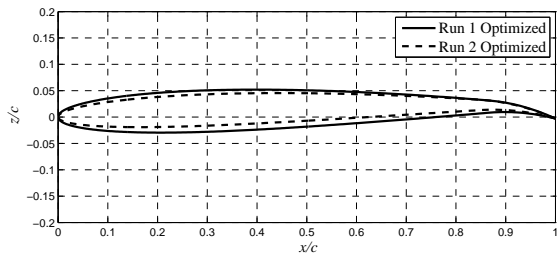
Comparing runs 1 and 2, we note that although starting from different initial designs the optimized designs show similarities in two of three design variables, the maximum camber  $m$  and maximum camber location  $p$ . The third, the airfoil thickness  $t/c$  differs by approximately 2%. The shock on the mid wing has been moved aft on both the upper and the lower sur-

Table 1: Numerical comparison of Run 1 and Run 2, initial and optimized designs. The ratio of the high-fidelity model evaluation time to the low-fidelity is 34.

Variable	Initial		Optimized	
	Run 1	Run 2	Run 1	Run 2
$m$	0.0200	0.0259	0.0200	0.0232
$p$	0.7000	0.8531	0.8725	0.8550
$t/c$	0.0628	0.0750	0.0793	0.0600
$C_L$	0.2759	0.3426	0.3047	0.3388
$C_D$	0.0241	0.0344	0.0311	0.0307
$C_L/C_D$	11.4481	9.9593	9.7974	11.0358
$A$	0.0422	0.0505	0.0534	0.0404
$N_c$	-	-	50	50
$N_f$	-	-	8	7
Total Cost	-	-	< 10	< 9



(a) Initial.



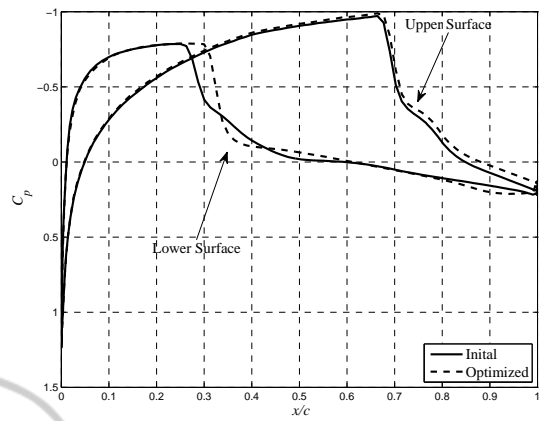
(b) Optimized.

Figure 7: A comparison of Run 1 and Run 2, initial and optimized designs. (a) Initial design comparison, and (b) Optimized comparison. Run 1 is shown with a solid lines (-), and Run 2 with dashed lines (- -).

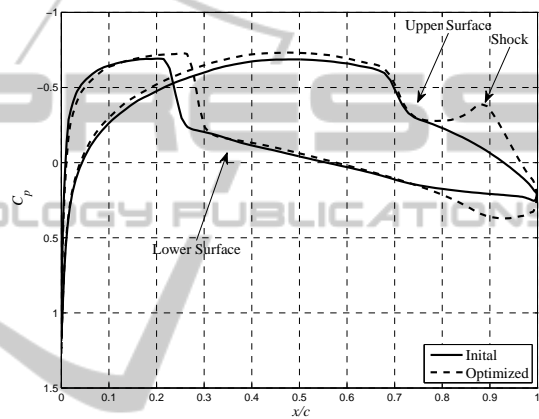
faces. Also, a second shock as formed near the tip on the upper surface. This causes the drag rise, as well as an increase in lift since the pressure distribution has opened up, as can be seen from Fig. 8.

## 5 CONCLUSIONS

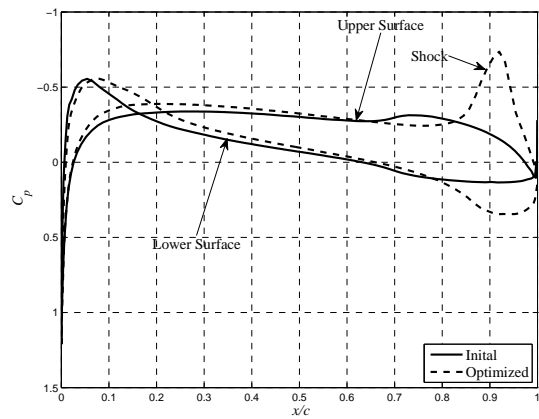
A robust and efficient aerodynamic design optimization methodology for wings using high-fidelity CFD models has been presented. Our approach exploits a cheap surrogate model to obtain an approximate optimum design of an expensive high-fidelity CFD



(a)  $y/(b/2) = 0.2$ .



(b)  $y/(b/2) = 0.65$ .



(c)  $y/(b/2) = 0.95$ .

Figure 8: Pressure distributions of the initial and optimized design of Run 1 at  $y/(b/2) =$  (a) 0.2, (b) 0.65, and (c) 0.95, where  $M_\infty = 0.8395$  and angle of attack  $\alpha = 3.06^\circ$ . Initial design is shown with a solid line (-) and the optimum design with a dashed line (- -).

model. The surrogate model is constructed using a corrected second-order polynomial approximation model derived from low-fidelity CFD model data. The correction is performed using the output space

mapping technique. The space mapping correction is applied both to the objectives and the constraints, ensuring zero-order consistency and a perfect alignment between the surrogate and the high-fidelity model. To our knowledge, this is the first application of the space mapping methodology used in conjunction with low-fidelity approximation models in aerodynamic shape optimization. The proposed approach performs well and optimized designs are obtained using only a few high-fidelity model evaluations.

## ACKNOWLEDGEMENTS

This work was funded by The Icelandic Research Fund for Graduate Students, grant ID: 110395-0061.

## REFERENCES

- Abbott, I. and Von Doenhoff, A. (1959). *Theory of wing sections: including a summary of airfoil data*. Dover.
- Alexandrov, N. and Lewis, R. (2001). An overview of first-order model management for engineering optimization. *Optimization and Engineering*, 2(4):413–430.
- ANSYS (2010). *ANSYS FLUENT Theory Guide*. ANSYS, Southpointe 275 Thecnology Drive Canonburg PA 15317, release 13.0 edition.
- Bandler, J., Cheng, Q., Dakroury, S., Mohamed, A., Bakr, M., Madsen, K., and Sondergaard, J. (2004). Space mapping: the state of the art. *Microwave Theory and Techniques, IEEE Transactions on*, 52(1):337–361.
- Echeverria, D. and Hemker, P. (2005). Space mapping and defect correction. *Computational Methods in Applied Mathematics*, 5(2):107–136.
- Forrester, A. and Keane, A. (2009). Recent advances in surrogate-based optimization. *Progress in Aerospace Sciences*, 45(1-3):50–79.
- Haikin, S. (1998). *Neural Networks: A Comprehensive Foundation*. Prentice Hall.
- Journel, A. and Huijbregts, C. (1978). *Mining geostatistics*. Academic press.
- Koziel, S., Cheng, Q., and Bandler, J. (2008). Space mapping. *Microwave Magazine, IEEE*, 9(6):105–122.
- Koziel, S., Ciaurri, D. E., and Leifsson, L. (2011). Surrogate-based methods. In *Computational optimization and applications in engineering and industry*, volume 359. Springer.
- Koziel, S. and Leifsson, L. (2012). Knowledge-based airfoil shape optimization using space mapping. In *30th AIAA Applied Aerodynamics Conference*.
- Leifsson, L. and Koziel, S. (2011a). Airfoil shape optimization using variable-fidelity modeling and shape-preserving response prediction. In *Comp. Opt., Methods and Algorithms*, volume 356. Springer.
- Leifsson, L. and Koziel, S. (2011b). Variable-fidelity aerodynamic shape optimization. In *Comp. Opt., Methods and Algorithms*, volume 356. Springer.
- Minsky, M. and Papert, S. (1969). *Perceptrons: An introduction to computational geometry*. The MIT Press, Cambridge, MA.
- NASA (2008). Onera-m6-wing validation case. In <http://www.grc.nasa.gov>.
- O’Hagan, A. and Kingman, J. (1978). Curve fitting and optimal design for prediction. *Journal of the Royal Statistical Society. Series B (Methodological)*.
- Queipo, N., Haftka, R., Shyy, W., Goel, T., Vaidyanathan, R., and Kevin Tucker, P. (2005). Surrogate-based analysis and optimization. *Progress in Aerospace Sciences*, 41(1):1–28.
- Raymer, D. (2006). *Aircraft design: a conceptual approach*. American Institute of Aeronautics and Astronautics.
- Robinson, T., Willcox, K., Eldred, M., and Haimes, R. (2006). Multifidelity optimization for variable-complexity design. In *Proceedings of the 11th AIAA/ISSMO Multidisciplinary Analysis and Optimization Conference, Portsmouth, VA*.
- Schmitt, V. and Charpin, F. (1979). Pressure distributions on the onera-m6-wing at transonic mach numbers. *Experimental Data Base for Computer Program Assessment*, Report of the Fluid Dynamics Panel Working Group 04, AGARD AR 138, May 1979.
- Simpson, T., Poplinski, J., Koch, P., and Allen, J. (July 2001). Metamodels for computer-based engineering design: survey and recommendations. *Engineering with computers*, 17(2):129–150.
- Smola, A. and Schölkopf, B. (2004). A tutorial on support vector regression. *Statistics and computing*, 14(3):199–222.
- Søndergaard, J. (2003). *Optimization using surrogate models by the space mapping technique*. PhD thesis, PhD. Thesis, Technical University of Denmark, Informatics and mathematical modelling.
- Tannehill, J., Anderson, D., and Pletcher, R. (1997). *Computational fluid mechanics and heat transfer*. Taylor & Francis Group.
- Wild, S., Regis, R., and Shoemaker, C. (2008). Orbit: Optimization by radial basis function interpolation in trust-regions. *SIAM Journal on Scientific Computing*, 30(6):3197–3219.
- Zhu, J., Bandler, J., Nikolova, N., and Koziel, S. (2007). Antenna optimization through space mapping. *Antennas and Propagation, IEEE Transactions on*, 55(3):651–658.